CDDpress

www.nature.com/cddis

ARTICLE OPEN

STAT6 inhibits ferroptosis and alleviates acute lung injury via regulating P53/SLC7A11 pathway

Youjing Yang[1,3], Yu Ma[1,3], Qianmin Li[2], Yi Ling[2], Yujia Zhou[2], Kaimiao Chu[2], Lian Xue[2] and Shasha Tao[1,2]✉

Compelling evidences have revealed the emerging role of ferroptosis in the pathophysiological process of acute lung injury (ALI), but its modulation is not clear. Here, we identified that STAT6 acted as a critical regulator of epithelium ferroptosis during ALI. Firstly, STAT6 expression and activity were increased in the ALI mice models caused by crystalline silica (CS), LPS and X-ray exposure. Followed by confirming the contribution of ferroptosis in the above ALI with ferrostatin-1 and deferoxamine intervention, bioinformatic analyses revealed that STAT6 expression was negatively correlated with ferroptosis. Consistently, lung epithelium-specific depletion of STAT6 in mice or STAT6 knockdown in cultured epithelial cells exacerbated ferroptosis in the above ALI. While overexpression of STAT6 in lung epithelial cells attenuated the ferroptosis. Mechanistically, SLC7A11 is a typical ferroptosis-related gene and negatively regulated by P53. CREB-binding protein (CBP) is a critical acetyltransferase of P53 acetylation, showing valuable regulation on targets' transcription. Herein, we found that STAT6 negatively regulates ferroptosis through competitively binding with CBP, which inhibits P53 acetylation and transcriptionally restores SLC7A11 expression. Finally, pulmonary-specific STAT6 overexpression decreased the ferroptosis and attenuated CS and LPS induced lung injury. Our findings revealed that STAT6 is a pivotal regulator of ferroptosis, which may be a potential therapeutic target for the treatment of acute lung injury.

Cell Death and Disease (2022)13:530 ; https://doi.org/10.1038/s41419-022-04971-x

INTRODUCTION

Acute lung injury (ALI) is a common clinical syndrome caused by both pulmonary and extra-pulmonary factors, and its most severe form ARDS (acute respiratory syndrome) causes high morbidity and mortality with no effective targeted intervention [1–3]. Previous studies have confirmed that inflammation, coagulation and oxidative stress play important role in the pathogenesis of ALI, which lead to inflammatory cells infiltration, pulmonary edema, arterial hypoxemia, finally results in dysfunction of lung tissue [4, 5]. We also reported that attenuation of oxidative stress and inflammatory response could alleviate the pathological condition of lung injury [6, 7]. Noteworthy, recent studies found that iron mobilization and decompartmentalization have a pathogenic role in both animal models and human cases of ALI, which reveals the contribution of ferroptosis to ALI [8].

Ferroptosis is an iron-dependent new programmed cell death, which is quite different from other classical programmed cell death, including apoptosis, necroptosis, senescence and autophagy both in morphology and biological properties [9, 10]. Hitherto a series studies have revealed that ferroptosis is involved in various diseases, such as tumor, nervous system disease and infection since it was initially proposed by Dixon et al. in 2012 [11–13]. Generally, ferroptosis can be triggered by physiological conditions such as high extracellular glutamate, cystine deprivation, amino acid starvation. It can also be induced through inhibiting system Xc^- (Cystine/glutamate transporter), GPX4 (glutathione peroxidase 4). Oppositely, ferroptosis can be suppressed by iron chelators (e.g., deferoxamine) and lipophilic antioxidants (e.g., ferrostatin-1) and inhibition of ferroptosis could diminish related clinical symptoms [14–17]. The mechanisms underlying the regulation of ferroptosis have involved multiple aspects, exemplified by autophagy, iron metabolism, and reactive oxygen species (ROS) metabolism et al. [18–20]. Remarkably, system Xc^- as the unique antioxidant has attracted extensive concern of scholars.

Solute carrier family 7 member 11 (SLC7A11) is one of the subunits of the system Xc^-, showing key modulation of iron overload-ferroptosis by transporting extracellular cysteine [12, 21]. Suppressing SLC7A11 reduced cystine uptake, which led to the deactivation of cystine-dependent glutathione peroxidase, enhanced intracellular lipid peroxidation and ferroptosis [22, 23]. Recently, it was reported that SLC7A11 is one of the critical targets of P53, and P53 could promote ferroptosis by inhibiting the uptake of cysteine [24–26]. Studies further confirmed that acetylation modulation of P53 is needed for the inhibition, and an acetylation defective mutant P53 with the specific mutated lysines to arginine residues could restore the SLC7A11 expression and improve the ferroptosis [27]. Therefore, targeting P53/SLC7A11 signaling may be a considered therapeutic approach to reverse ferroptosis during ALI.

Signal transducer and activators of transduction 6 (STAT6) is a key regulator in innate immune response, which mediates direct

[1]Chongqing University Central Hospital&Chongqing Emergency Medical Center, No.1 Jiankang Road, Yuzhong District, Chongqing 400014, China. [2]School of Public Health, Medical College of Soochow University, 199 Ren'ai Road, Suzhou 215123, China. [3]These authors contributed equally: Youjing Yang, Yu Ma. ✉email: sstao@suda.edu.cn

Edited by Professor Massimiliano Agostini

Received: 8 November 2021 Revised: 16 May 2022 Accepted: 25 May 2022
Published online: 06 June 2022

repression of inflammatory enhancers and regulates activation of alternatively polarization [28]. Series studies have showed that regulation of STAT6 could suppress inflammatory response by promoting M2 macrophages polarization [29–31]. Although the role of STAT6 in the field of immuno-regulation has been well studied, the function in intrinsic cells like lung epithelium remains unclear. In this study, we identified the indispensable role of STAT6 in maintaining alveolar epithelial cells homeostasis during ALI, moreover we originally investigated its novel regulatory mechanism of ferroptosis.

MATERIALS AND METHODS

Chemicals, antibodies and cell culture

Crystalline Silica particles (Quartz DQ 12) were purchased from Doerentrup Quarz GmbH (Germany). Lipopolysaccharide (LPS, SI732) was purchased from Beyotime (Shanghai, China). Ferrostatin-1 (Ferr-1, T6500) was purchased from TargetMol (MA, USA). Deferoxamine (DFO, GC13554), Erastin (GC16630), and RSL3 (GC12431) were purchased from Glpbio (Shanghai, China). Nicotinamide (NAM, 72340) was from Sigma Aldrich. TrichostatinA (TSA, S1045) was purchased from Selleck (Shanghai, China). Primary antibodies against STAT6 (sc-374021), p-STAT6 (sc-136019), PTGS-2 (sc-52972), P53 (sc-126), P21 (sc-6246), CBP (sc-32244), HA (sc-7392), Histone H3 (sc-517576), and β-actin (sc-47778) were from Santa Cruz (Texas, USA), and against SLC7A11 (AF7992) was from Beyotime (Shanghai, China). Antibody against 8-oxo-dG (#3154-MC-050) was from Trevigen (Gaithersburg, MD). Primary antibodies against Flag (#14793) and acetylated-lysine (#9441S) were purchased from Cell Signaling Technology (Danvers, MA, USA). Antibody against 4-hydroxynonenal (4-HNE) was from Bioss (Beijing, China). HRP-conjugated secondary antibodies were purchased from Immunoway (Plano, TX, USA; anti-mouse:RS0001, anti-rabbit: RS0002). Alexa Fluor 488 anti-mouse (ab150113, Abcam, UK) and Alexa Fluor 594 anti-rabbit antibodies (ab15008, Abcam, UK) and DAPI (Solarbio, China, C0065) were used in immunofluorescence (IF) staining. Human THP-1 acute monocytic leukemia cells and immortalized human bronchial epithelial HBE cells were purchased from ATCC (Manassas, VA, United States). THP-1 cells were cultured in RPMI1640 containing 10% fetal bovine serum (FBS, Hyclone), 1% penicillin/streptomycin (Invitrogen) and differentiated by 5 ng/ml phorbol-12-myristate-13-acetate (PMA, Sigma), while HBE cells were cultured in Dulbecco modified eagle medium (DMEM) supplemented with 10% FBS and 1% penicillin/streptomycin. The cells were maintained at 37 °C in a humidified incubator containing 5% CO_2.

Animal experiments

C57BL/6, $STAT6^{flox/flox}$ and $Sftpc^{Cre}$ mice were purchased from Cyagen Biosciences (Guangzhou, China). $STAT6^{flox/flox}$ mice were crossed with $Sftpc^{Cre}$ mice to generate lung epithelium-specific STAT6 knockout ($STAT6^{cKO}$) mice. All mice received standard laboratory diet and maintained in 12 h light/dark cycle, climate-controlled and pathogen-free rooms. Mice handling in this study followed the Guide for the Care and Use of Laboratory Animals and the study protocols were approved by Soochow University Institutional Animal Care and Use Committee. Six to eight weeks old gender-matched wildtype and knockout mice from the same litter were selected randomly to indicated groups based on genotypes. Two in vivo studies were performed as follows: a) Mice were randomly divided into eight groups ($n = 6$ per group): (i) Control group (Ctrl), (ii) Crystalline Silica group (CS), (iii) Crystalline Silica and Ferrostatin-1 group (CS + Ferr-1), (iv) Crystalline Silica and Deferoxamine group (CS + DFO), (v) Lipopolysaccharide group (LPS), (vi) Lipopolysaccharide and Ferrostatin-1 group (LPS + Ferr-1), (vii) Lipopolysaccharide and Deferoxamine group (LPS + DFO), (viii) X-ray groups (X-ray). For the models of CS and LPS exposure, mice were anesthetized and intratracheally instilled with CS suspensions (3 mg/50 μl) or LPS (1 mg/kg). For the models of CS + Ferr-1/DFO, mice were intraperitoneally injected with Ferr-1 (1.25 μmol/kg) or intranasal instilled with DFO (10 mg/kg) for 7 consecutive days after CS instillation. For the models of LPS + Ferr-1/DFO, mice were pretreated with Ferr-1 or DFO for 2 consecutive days and then intratracheally instilled with LPS. Mice were sacrificed 24 h after LPS instillation. For the X-ray exposure model, mice were exposed to ionizing radiation (IR) at 20 Gy, which was delivered at the dose rate of 2 Gy/min and a source skin distance of 51 cm by an X-ray generator (Model X-RAD320iX; Precision X-Ray, Inc., North Branford, CT, USA), and sacrificed 3 days after radiation. All mice were euthanized and bronchoalveolar lavage fluid (BALF) was obtained by lavaging the whole lung with PBS (Invitrogen). b) STAT6 rescue in vivo study: Mice were intratracheally instilled with lenti-Veh or lenti-mouse STAT6 one week ago and at day 0 respectively. Mice from CS group were intratracheally instilled with CS at day 0 together with lentivirus administration. Model of LPS were intratracheally instilled with LPS 5 days after the second instillation of virus. All mice were sacrificed at day 7, and all biological samples were collected for following analyses.

Hematoxylin and Eosin (H&E), Immunohistochemistry (IHC)

Lung tissues were fixed in 4% paraformaldehyde and the slides (4μm) were cut. H&E staining and lung injury scoring were performed as previously description [32–34]. For IHC staining, the lung sections were incubated with primary antibodies at 4 °C overnight. After washing three times with PBS, the slides were then stained with secondary antibody. The results were visualized by light macroscope (Leica DM 2500, Wetzlar, Germany).

RNA extraction and quantitative real-time PCR (qRT-PCR)

Total RNA was extracted from lung tissues and cells using TRIzol reagent (CWBIO, Beijing, China). Equal amounts of RNA were reverse transcribed using HiFiScript cDNA synthesis kit according to the manufacturer's instructions (CWBIO, Beijing, China) in 8-strip tubes (#404001, Nest, China). The real-time polymerase chain reaction was carried out using SYBR Green PCR Matser Mix (CWBIO, Beijing, China) according to the manufacturer's protocol. The sequence of primers used in this study were listed in Supplementary Table 1.

Immunoblot analysis, nuclear and cytoplasmic protein extraction, and Immunoprecipitation

For immunoblot analysis, lung tissues and cells were lysed with RIPA buffer and total protein content was quantified with bicinchoninic acid (BCA) protein assay kit (Fdbio science, Hangzhou, China). The extraction of nuclear and cytoplasmic protein was performed according to the manufacturer's instructions (Fdbio science, Hangzhou, China). Briefly, lung tissues were homogenized and cells were lysed with reagent A in the kit. After vortex and incubation 20 min on ice, reagent B (1/20 volume of reagent A) was added. Followed by vortex and 1 min incubation on ice, the tissue or cell mixture were centrifuged 12,000 rpm, 4 °C for 15 min. Then the supernatant was harvested as cytoplasmic protein, and the precipitate was added with reagent N. After vortex and incubation on ice for 40 min, the precipitate was centrifuged and the supernatant was collected as nuclear protein. The lysates were denatured and electrophoresed through SDS-polyacrylamide gel and subjected to immunoblot analysis. For immunoprecipitation, cells were harvested in RIPA buffer (Fdbio science, Hangzhou, China) and pre-clear with 10 μl protein A agarose beads. After centrifugation, the supernatant was collected and added with indicated antibodies (1 μg) and rotation in 4 °C for 2 h. Then, the samples were added with another 20 μl protein A agarose beads and rotation in 4 °C overnight. Immunoprecipitated complexes were subjected to immunoblot with the indicated antibodies. Relative immunoblot bands were compared using the prestained protein marker (Vazyme Biotech Co.,Ltd, MP102-01) and Thermo Scientific PageRuler Prestained Protein Ladder (#26617).

Transfection of shRNA and cDNA

Cells were transfected with vectors containing the indicated sh-RNA or with specific genes expression by PEI40000 reagent (40816ES03, Yeasen, China) according to the manufacturer's instructions. Briefly, 1 μg of vector with 3 μl PEI40000 were separately mixed with 100 μl Opti-medium (Invitrogen) and combined with each other. After 20 min incubation, the mixtures were added into the cells. Cells were used for the following indicated studies after 24 or 48 h incubation (37 °C; 5% CO_2).

Response element (RE) of P53 on SLC7A11 promoter cloning

The sequence of human SLC7A11 promoter (−39 to −16) was synthetized in GENEWIZ and cloned into PGL3-Basic vector with KpnI and BglII by a standard cloning protocol [35].

Data collection

All data were downloaded from the National Center of Biotechnology Information (NCBI) Gene Expression Omnibus (GEO) (https://www.ncbi.nlm.nih.gov/geo/) [36]. The microarray-based expression data of lung tissue from rats with one week crystalline silica treatment were collected from GSE32147. Lung samples from wild type (WT) and $Stat6^{-/-}$ mice were

obtained from GSE1438. Raw count data of normal human lung tissue samples were obtained from the Genome Tissue Expression (GTEx) database [37].

Bioinformatics analysis

Limma package was used to identify and filter differentially expressed genes (DEGs) between different groups in each of the datasets [38, 39]. In addition, R packages ggplot2 and Complex Heatmap were employed to visualize the DEGs [40]. The Gene sets and Gene Set Enrichment Analysis (GSEA) was performed by GSEA 4.1.0 to find possible functions of STAT6. Gene set enrichment analysis (GSEA) was carried out to verify the ferroptosis-related functions and explore the potential signaling pathway leading to ferroptosis between mice with high and low STAT6 expression [41, 42]. Protein-protein interactions (PPI) was performed by Retrieval of Interacting Genes/Proteins (STRING) to explain the potential regulation of STAT6 on ferroptosis [43]. The regulatory relationship between genes was visualized by Cytoscape 3.8.2 [44].

Indirect immunofluorescence

Cells were seeded on glass coverslips (Thermo Fisher Scientific, Waltham, MA, USA). Cells were fixed with chilled methanol for 15 min, then coverslips were incubated by the primary antibodies and the respective secondary antibodies for 50 min each. Finally, the coverslips were mounted with antifade mounting solution (Invitrogen, Carlsbad, CA, USA), and images were acquired and observed with a fluorescence microscope (Leica DM 2500, Wetzlar, Germany).

Detection of GSH, MDA and iron content

The content of GSH was detected by the corresponding commercial kit (A006-2-1, Nanjing Jiancheng Biotechnology, China) and MDA were measured using the Lipid Peroxidation MDA Assay Kit (S0131, Beyotime, China). The content of iron was measured by Iron Colorimetric Assay Kit (E-BC-K139-M, Elabscience, China). All kits were used under the manufacturer's instructions.

Cell viability assay

Cell viability was measured by MTT assay. 3-(4, 5-dimethylthiazol-2-yl)-2, 5-diphenyltetrazolium bromide was purchased from Sigma-Aldrich. Briefly, approximately 1×10^4 cells per well were seeded in a 96-well plate for 48 h with multiply treatments. 20 µl MTT (2 mg/ml) in PBS solution was added and incubated for 3 h at 37 °C. The supernatant was removed and 100 µl of isopropanol/HCl was added. The absorbance at 570 nm was measured with a multifunctional microplate reader (Molecular Devices, USA).

Dual-luciferase reporter assay

Cells were seeded in 24-wells plate and transfected with SLC7A11 promoter and other target plasmids using PEI40000 reagent (40816ES03, Yeasen, China). Luciferase activity was then evaluated with Dual Luciferase Reporter Gene Assay Kit (RG027, Beyotime, China) following the manufacturer's instructions.

Chromatin immunoprecipitation (ChIP)

HBE cells were fixed with formaldehyde, collected in PBS and re-suspended in SDS buffer. Cells were subsequently sonicated on ice. Following sonication, the lysates were then pre-cleared at 4 °C with protein A agarose, and then incubated with indicated antibodies and protein A agarose overnight. Antibody bead complexes were washed and eluted with corresponding buffer. Then cross-links were reversed and DNA was recovered. Then amounts of DNA in the complex were quantified by real-time PCR. Fold enrichment was calculated as ChIP signals divided by no antibody control and normalized to input. The primer sequence of human SLC7A11 used for ChIP was listed below:

Forward: AGGCTTCTCATGTGGCTGAT,
Reverse: AATAGCCACCAGCCTCTTCT

Terminal deoxynucleotidyl transferase mediated dUTP nick end-labeling (TUNEL) assay

Lung sections or HBE cells were washed and fixed with 4% paraformaldehyde at room temperature. After incubation with proteinase K, lung sections or cells were subjected to TUNEL detection kit (Vazyme Biotech Co.,Ltd, A111). Samples were visualized by a fluorescence microscope (Leica DM 2500, Wetzlar, Germany).

Lactate dehydrogenase (LDH) assay

LDH assay is usually used to measure the tissue or cell injury [45]. The LDH of mice BALF or of HBE cells was measured by the LDH assay kit (A020-2, Nanjing jiancheng Biotechnology, China) according to manufacturers' instructions. Briefly, an aliquot of the BALF and HBE cell lysis were used to incubated with the reagents supplied by the above kit. After incubation for 5 min, absorbance was measured at 450 nm.

Statistics

The investigators were blinded to group allocation. All related data were presented as means ± SD of three independent experiments performed in triplicate. GraphPad Prism 8.0 and R statistical software were performed for graphics and statistical analyses. For comparison between two groups, unpaired Student's *t* tests were applied. Multiple comparisons were analyzed using one-way ANOVA with *Bonferroni's* correction, and variance was similar between groups. $p < 0.05$ was considered statistically significant.

RESULTS

STAT6 expression and activation are upregulated along with ferroptosis induction during ALI

To identify the role of ferroptosis in ALI, CS- and LPS- induced ALI mice models were established with Ferr-1 and DFO intervention. As shown in Supplementary Figs. S1A–D and S2A–D, PTGS-2 expression and iron content were both induced after CS and LPS exposure, which were inhibited by Ferr-1 and DFO administration. H&E staining showed obvious inflammatory cell infiltration and thickened alveolar septum in the lung tissues of CS- and LPS-treated mice, which were attenuated by Ferr-1 and DFO (Supplementary Figs. S1E,F and S2E,F). Next oxidative stress, as a critical component in the process of ALI was detected as well. As shown in Supplementary Figs. S1G–J and S2G–J, mice lung tissues were detected decreased GSH content but increased MDA content after CS and LPS exposure. Meanwhile, CS- and LPS- instillation also caused oxidative DNA damage as reflected by the upregulated 8-oxo-dG level (Supplementary Fig. S1K,L). Consistently, mice instilled with CS and LPS were also detected increased levels of protein and LDH in BALF (Supplementary Fig. S2K–N). Fortunately, all these damages above could be alleviated by Ferr-1 or DFO intervention (Supplementary Figs. S1 and S2). Additionally, TUNEL assay were performed to confirm whether other forms of cell death occurred in the ALI. The result of TUNEL staining showed that only few positive stained cells were observed after treated with CS or LPS (Supplementary Fig. S4). These data indicates that ferroptosis would be the major contributor to stimuli-induced ALI.

Along with the induction of ferroptosis, STAT6 mRNA expression was upregulated with the stimuli (Fig. 1A). STAT6 protein level and activation were detected as well. The result showed that the protein levels of STAT6 and p-STAT6 were both increased after the stimuli exposure (Fig. 1B). Meanwhile, IHC staining showed that CS, LPS and X-ray exposure promoted the STAT6 translocation into the nuclear (Fig. 1C, Supplementary Fig. S3). Additionally, the extracted nuclear protein lysis was subjected to immunoblot and the result indicated that STAT6 was activated, manifesting as its increased expression in the nucleus (Fig. 1D). These data above indicates that STAT6 signals are increased along with the induction of ferroptosis during the above ALI.

Ablation of STAT6 in pulmonary epithelium exacerbates ferroptosis and aggravates lung injury

To investigate the relationship between STAT6 and ferroptosis, we grouped CS-induced lung injury animal models (GSE32147) according to the median STAT6 expression and compared their gene expression profiles. A total of 826 genes (437 upregulated

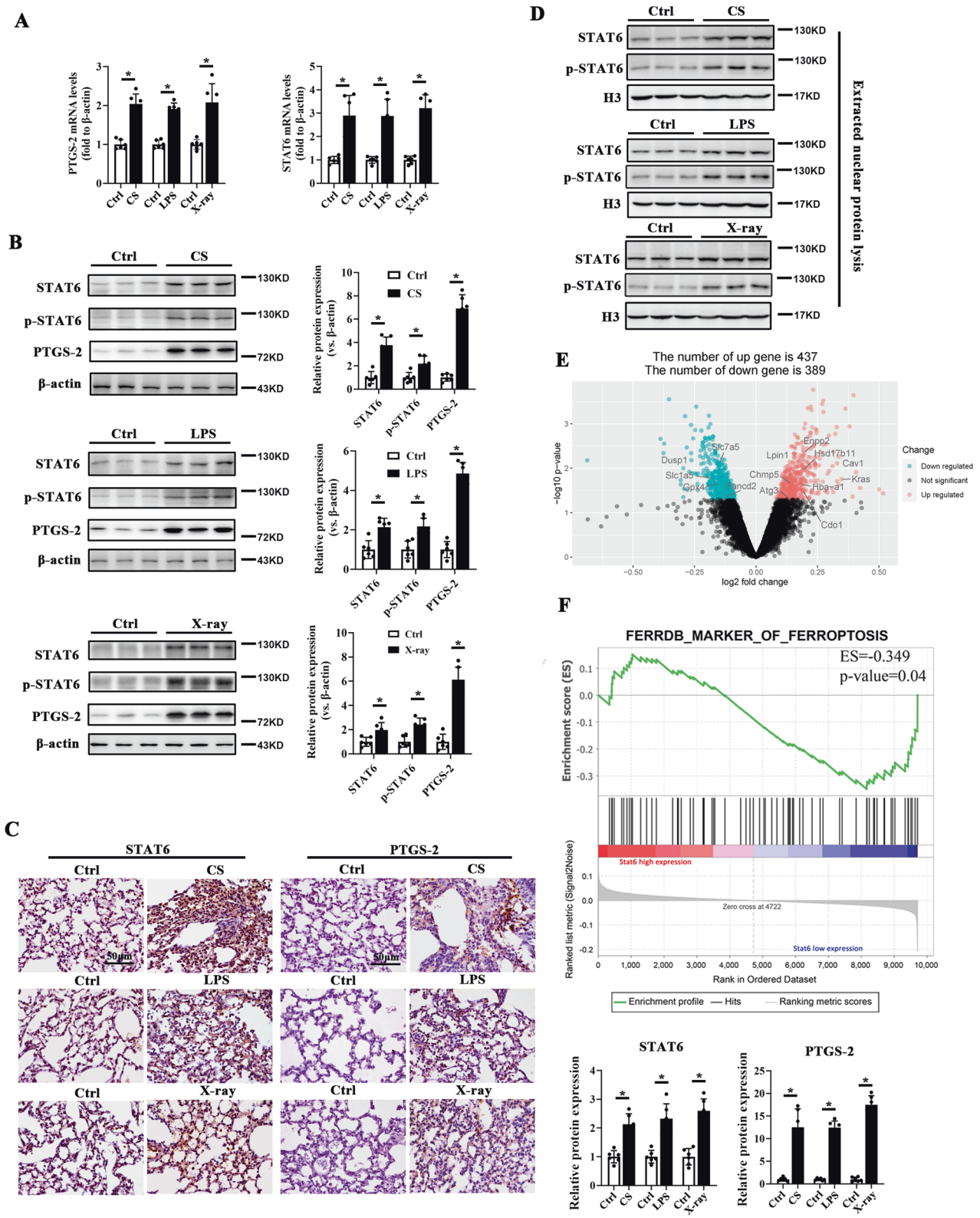

Fig. 1 STAT6 is activated in CS, LPS and X-ray induced ferroptosis of acute lung injury. A The mRNA levels of PTGS-2 and STAT6 in indicated mice lung tissue were determined by qRT-PCR. **B** Lung tissue lysates from indicated group of mice were subjected to immunoblot analysis with the quantification on the right panel. **C** Representative photographs showed STAT6 and PTGS-2 staining in lung tissue from indicated groups. **D** The expression of STAT6 in indicated extracted nuclear protein. **E** Volcano plot showed differential expressed genes in rats with high and low Stat6 expression with ferroptosis-related genes labeled. **F** GSEA plot showed enrichment of "marker of ferroptosis" in STAT6 low expression group of rat. Data were expressed as means ± SD ($n = 6$, $^*p < 0.05$, Ctrl *vs.* treatment).

and 389 downregulated) was found to be significantly changed, which were labeled in the volcano map (Fig. 1E). The association between STAT6 and ferroptosis in lung tissue was further investigated through GSEA analysis. Marker genes of ferroptosis were observed significantly enriched in lung tissues with low expression of STAT6 (Fig. 1F). These results indicate that STAT6 is negatively correlated with ferroptosis in ALI.

Next, lung epithelium-specific STAT6 deficient mice ($STAT6^{cKO}$) generated by crossing $STAT6^{flox/flox}$ and $Sftpc^{cre}$ mice were also employed to build the ALI models. Tamoxifen was injected to induce the activity of cre accordingly [46]. The ratio of lung weight to body weight (LW/BW) were increased after CS instillation, and $STAT6^{cKO}$ mice exhibited even higher LW/BW than WT mice (Fig. 2A,B). H&E staining showed that CS instillation induced the inflammatory cells infiltration and cellular nodules in the lung tissue of WT and $STAT6^{cKO}$ mice, and STAT6 deficiency aggravated the inflammation (Fig. 2C). IHC staining of 8-oxo-dG showed that CS exposure caused oxidative DNA damage, which was exacerbated in $STAT6^{cKO}$ mice (Fig. 2D). Meanwhile, $STAT6^{cKO}$ mice were found to exhibit higher expression of PTGS-2 as identified by IHC staining, immunoblot and qRT-PCR analysis after CS instillation (Fig. 2D–F). Consistently, the downregulated GSH content caused by CS was further decreased in $STAT6^{cKO}$ mice, and the increased MDA, iron content and 4-HNE were further upregulated (Fig. 2G–J). All these data indicates that CS-induced ferroptosis are aggravated in $STAT6^{cKO}$ mice.

To verified whether STAT6 deficiency exacerbated ferroptosis is widely existed in ALI, LPS- and X-ray- induced ALI models were built as well. H&E staining showed that $STAT6^{cKO}$ mice exhibited more inflammatory cell infiltration and thickened alveolar septum (Supplementary Figs. S5A and S6A) compared with WT mice after stimuli. Similarly, the induced levels of 8-oxo-dG and PTGS-2 by stimuli were further increased in $STAT6^{cKO}$ mice lung tissues (Supplementary Figs. S5B, F and S6B, F). The suppressed content of GSH was even more decreased and the increased levels of MDA and iron accumulation were higher in $STAT6^{cKO}$ mice lung tissues (Supplementary Figs. S5C–E and S6C–E). These data indicates that STAT6 deficiency in the lung epithelium promotes ferroptosis and exacerbates lung injury.

STAT6 positively regulates SLC7A11 and suppresses ferroptosis

SLC7A11 is an critical ferroptosis related gene, and its expression was observed decreased in $STAT6^{cKO}$ mice with or without stimuli (Fig. 2E,F, Supplementary Figs. S5F and S6F). In order to identify the relationship between STAT6 and SLC7A11, the gene sets of STAT6 knockout mice were employed to apply GSEA to GTEx samples grouped by median SLC7A11 expression. In GSE1438, the 150 significant DEGs with the maximum log2FC were defined as genes negatively regulated by STAT6. Simultaneously, the 150 significant DEGs with the minimum log2FC were defined as genes positively regulated by STAT6. The expression of 300 DEGs selected into gene sets based on the expression profile of GSE1438 was shown in the heat map (Fig. 3A left). Among them, there were 77 upregulated genes and 98 downregulated genes finally mapped to homologous genes of homo sapiens. Then, GSEA revealed that genes negatively regulated by STAT6 were significantly enriched in SLC7A11 low expression group. Correspondingly, genes positively regulated by STAT6 were enriched in SLC7A11 high expression group (Fig. 3A right). These results suggest that SLC7A11 is positively correlated with STAT6 signaling.

To investigate the detail regulation of STAT6 on ferroptosis, the differentiated THP-1 cells were exposed with CS for 24 h and the cell culture medium was harvested to further treat HBE cells (Fig. 3B). CS medium treatment upregulated the expression of PTGS-2, which was further increased by silencing STAT6 but decreased by STAT6 overexpression (Fig. 3C, H, I). Consistently, STAT6 overexpression restored the cell viability and GSH content, while silencing STAT6 reversed these changes (Fig. 3D, E). Also, CS medium incubation dramatically increased the MDA and iron content, which was alleviated with STAT6 overexpression but exacerbated with STAT6 knockdown (Fig. 3F,G). The results above were consistently observed in the cells treated with LPS (Supplementary Fig. S7A–F). Additionally, the classical ferroptois inducer Erastin and RSL3 were also used to confirmed the role of STAT6 in regulating ferroptosis. It was shown that the induced content of iron and MDA was further increased and the decreased GSH level was further suppressed after inhibiting STAT6 (Supplementary Fig. S7G–I). Besides, SLC7A11 expression was decreased after CS medium or LPS treatment, which was restored with STAT6 overexpression but aggravated with STAT6 knockdown (Fig. 3H–I, Supplementary Fig. S7F). These results indicate that STAT6 restores the depressed SLC7A11 expression in ferroptosis and plays an important role in suppressing ferroptosis.

STAT6 downregulates P53 signaling to alleviate ferroptosis through decreasing its acetylation modification

To further explore the possible regulation mechanism of STAT6 on ferroptosis, we selected STAT6 and ferroptosis related proteins reported in literature to establish protein-protein interaction (PPI) network and calculate the top 10 genes as the hub genes indicated [47]. The network diagram showed that P53 is the only hub gene associated with STAT6 and was closely related to other nodes in the network, which indicated that STAT6 may regulate other ferroptosis through P53 (Fig. 4A). Next, we performed differential analysis separately on GTEx lung tissue data categorized by median STAT6 and P53 expression. The results demonstrated that there were 753 overlaps between significant differentially expressed grouped by STAT6 and P53 ($p < 0.05$) (Fig. 4B). Then, according to STAT6 expression level, the expression condition of 753 common DEGs in 68 GTEx samples was revealed in Fig. 4C, among which the genes related to oxidative stress, lipid metabolism and ferroptosis were annotated on the side strip. Additionally, we also found that P53 signaling pathway geneset from Kyoto Encyclopedia of Genes and Genomes (KEGG) database was significantly enriched in the group with low STAT6 expression by GSEA (Fig. 4D). These findings suggest that STAT6 attenuates ferroptosis in lung injury by negatively regulating P53 signaling.

Subsequently, the potential regulation of STAT6 on P53 signaling and its association with SLC7A11 were detected. HBE cells were transfected with STAT6 and P53 plasmid, then the cells were harvested and subjected to immunoprecipitation and immunoblot analysis. The results showed that there was no direct binding between STAT6 and P53, meanwhile the location of P53 was not affected by STAT6 (Supplementary Fig. S8A–C). Next the results of immunoprecipitation (Fig. 4E) and qRT-PCR (Fig. 4G) showed that the protein and mRNA levels of P21 as well as acetylated P53 but not P53 itself were dose-dependently decreased with STAT6 overexpression, which were increased by STAT6 inhibition oppositely. The expression of SLC7A11 was positively regulated by STAT6 in the cells. Besides, in order to confirmed that STAT6 specifically regulated the acetylation of P53, we additionally conducted the IP assay using the Ack-pan antibody to detect P53 expression, and the results consistently showed that STAT6 negatively regulated P53 acetylation (Supplementary Fig. S8D). Similarly, the protein levels of P53 acetylation and P21 were significantly increased in $STAT6^{cKO}$ mice lung tissues, while the protein expression of SLC7A11 was decreased compared to WT mice (Fig. 4F). Furthermore, we confirmed whether P53 acetylation regulated CS or LPS induced iron accumulation and lipid peroxidation. As shown in Supplementary Fig. S8F,G, induction of P53 acetylation using TSA/NAM [48] upregulated CS and LPS induced iron and MDA content, while suppressing P53 acetylation by silencing CBP downregulated the increased iron and MDA content. Taken together, the results suggest that STAT6 alleviates ferroptosis may be through inhibiting P53 acetylation to improve the expression of SLC7A11.

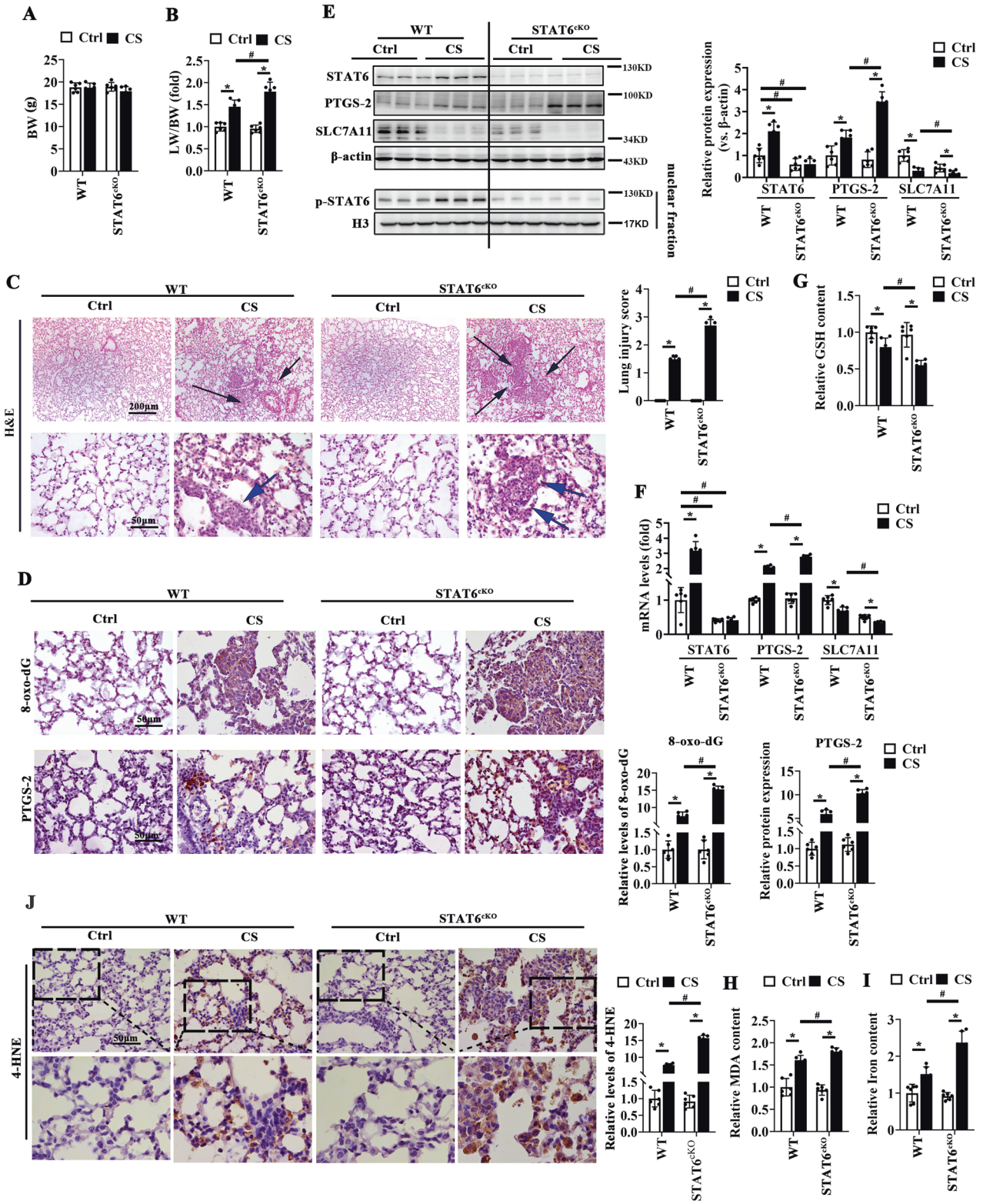

Fig. 2 STAT6 deficiency in lung epithelium aggravates CS-induced ferroptosis and lung injury. Wild type (WT) and lung epithelium-specific STAT6 deficiency mice (STAT6^{cKO}) mice were intratracheally instilled with CS and sacrificed 7 days later. **A** Body weight (BW) and **B** the ratio of lung weight to BW were determined. **C** Representative H&E-stained lung sections from WT and STAT6^{cKO} mice and lung injury score. (Black and blue arrows indicated inflammatory nodules and inflammatory cells infiltration respectively). **D** IHC staining of 8-oxo-dG and PTGS-2 of lung sections from indicated group were performed and quantified. Representative images from each group were shown. The protein expression (**E**) and mRNA **F** levels of STAT6, PTGS-2 and SLC7A11 in lung tissue were determined by western blot analysis and qRT-PCR assay. The relative GSH **G**, MDA (**H**) and Iron **I** content were measured by corresponding kit. **J** IHC staining of 4-HNE in lung sections from indicated group were performed and quantified. Representative images from each group were shown. The data were presented as means ± SD ($n = 6$, $^{*}p < 0.05$, Ctrl *vs.* CS; $^{\#}p < 0.05$, WT *vs.* STAT6^{cKO}).

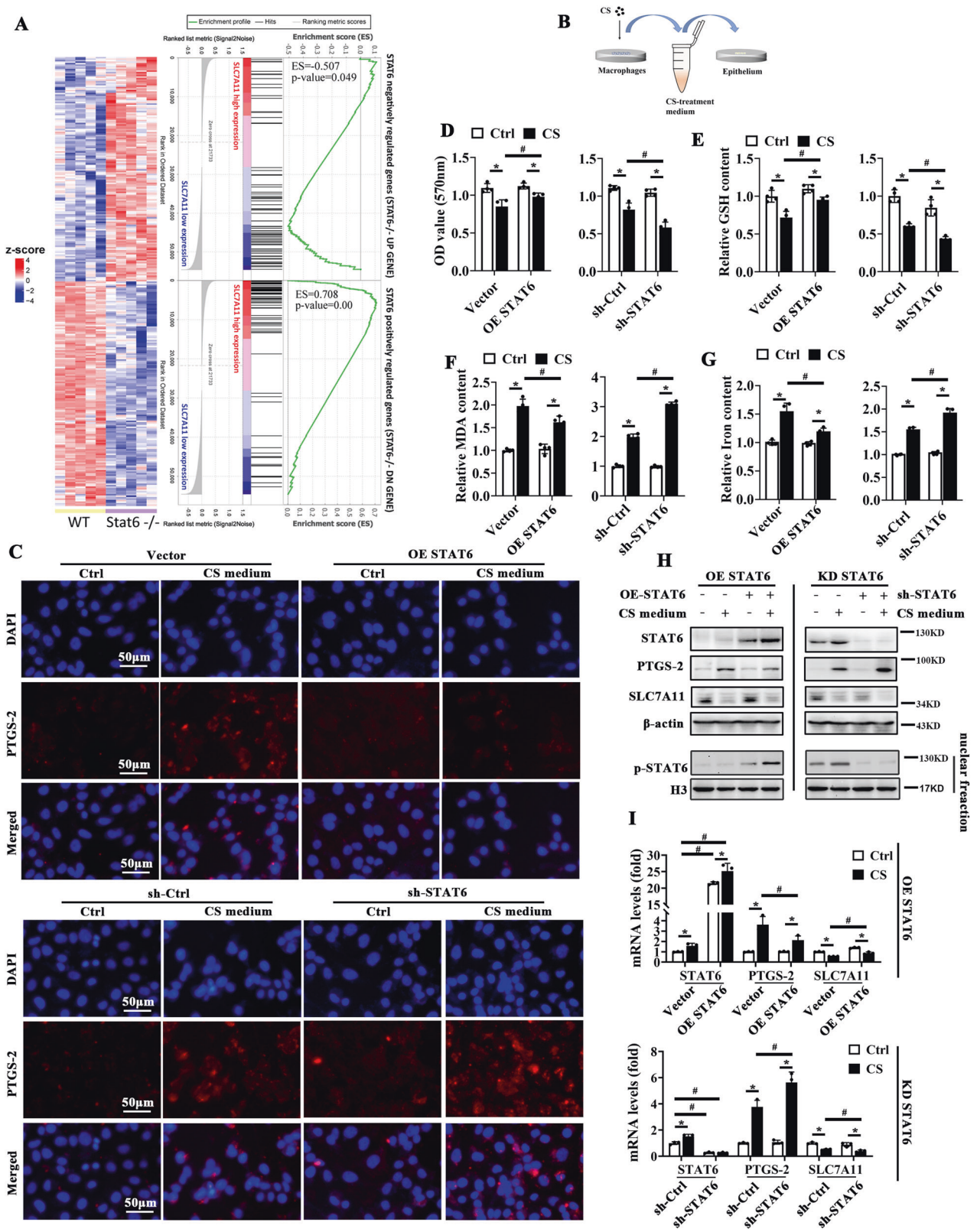

Fig. 3 STAT6 suppresses ferroptosis and positively regulates SLC7A11. A Left panel, heat map showed genes negatively or positively regulated by STAT6. Right panel, GSEA plot showed enrichment of "STAT6 negatively regulated genes" in SLC7A11 low expression group and "STAT6 positively regulated genes" in SLC7A11 high expression group. **B** The co-cultured system of macrophages and epithelium. HBE cells were transfected with sh-Ctrl or plasmid for STAT6 inhibition or overexpression and treated with CS-medium for 24 h. **C** Immunofluorescence staining of PTGS-2 in cells with indicated treatment. DAPI was used for nucleus staining. The cell viability **D**, GSH **E**, MDA (**F**) and Iron **G** content in cells were measured ($n = 4$). The protein (**H**) and mRNA (**I**) levels of STAT6, PTGS-2 and SLC7A11 were measured by immunoblot analyses and qRT-PCR assay ($n = 3$). The data were presented as means ± SD (*$p < 0.05$, Ctrl *vs*. CS; $^{\#}p < 0.05$, Vector/sh-Ctrl *vs*. OE-STAT6/sh-STAT6).

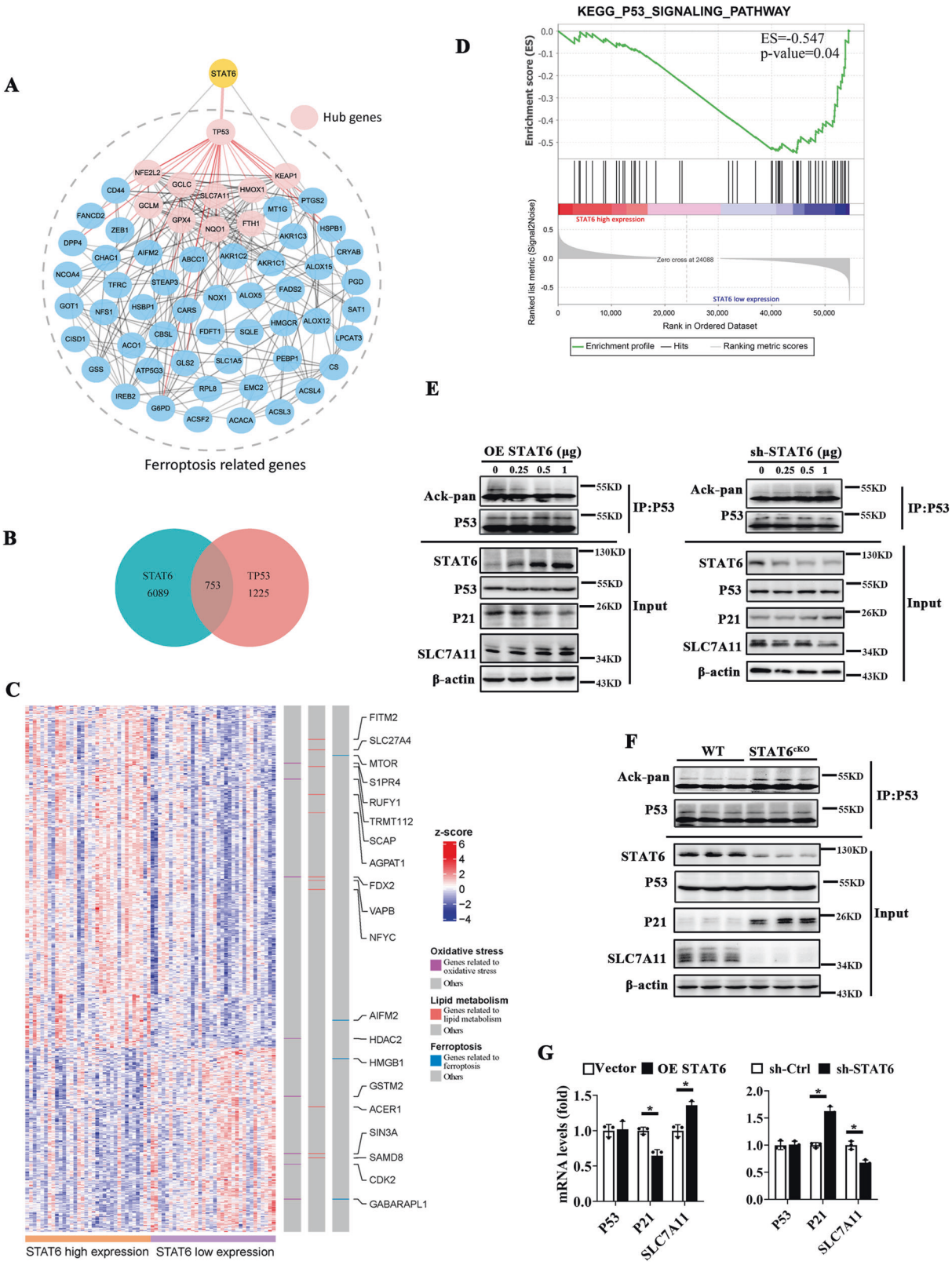

STAT6 competitively binds with CBP and restores the inhibition of P53 on SLC7A11 expression

To confirm that STAT6 regulates ferroptosis via P53, HBE cells transfected with P53 and STAT6 were subjected to analysis. In accordance with the results of Fig. 4, P53 overexpression aggravated CS-induced ferroptosis as determined by the increased level of PTGS-2 and decreased cell viability, which could be inversely improved by STAT6 overexpression (Fig. 5A,B). Consistently, CS-induced GSH inhibition (Fig. 5C), MDA generation (Fig. 5D), iron accumulation (Fig. 5E) and LDH release (Fig. 5F) were

Fig. 4 STAT6 downregulates P53 signaling pathway to alleviate the ferroptosis by decreasing its acetylation modification. A PPI network showed the relationship between STAT6 and ferroptosis related genes. Red nodes represented hub genes calculated by plugin Cytohubba. Red edges represented interactions between TP53 and its associated genes. **B**–**D** were performed upon GTEx lung tissue sample. **B** Venn diagram showed the overlap between 6089 genes that were significantly differentially expressed grouped by STAT6 and 1225 genes grouped by TP53. **C** Heat map showed the expression of 753 common DEGs in GTEx samples with genes associated with specific biological process annotated. **D** GSEA plot showed enrichment of KEGG term "P53 signaling pathway" in STAT6 low expression group. **E** HBE cells were transfected with indicated plasmid and harvested for immunoprecipitation and immunoblot analysis with the indicated antibodies. **F** The protein lysis of lung tissue from WT and STAT6^{cKO} mice were subjected to immunoprecipitation and immunoblot analysis with the indicated antibodies. **G** The mRNA levels of P53, P21, SLC7A11 were measured by qRT-PCR assay. ($n = 4$, $^{*}p < 0.05$, Vector/sh-Ctrl *vs*. OE-STAT6/sh-STAT6).

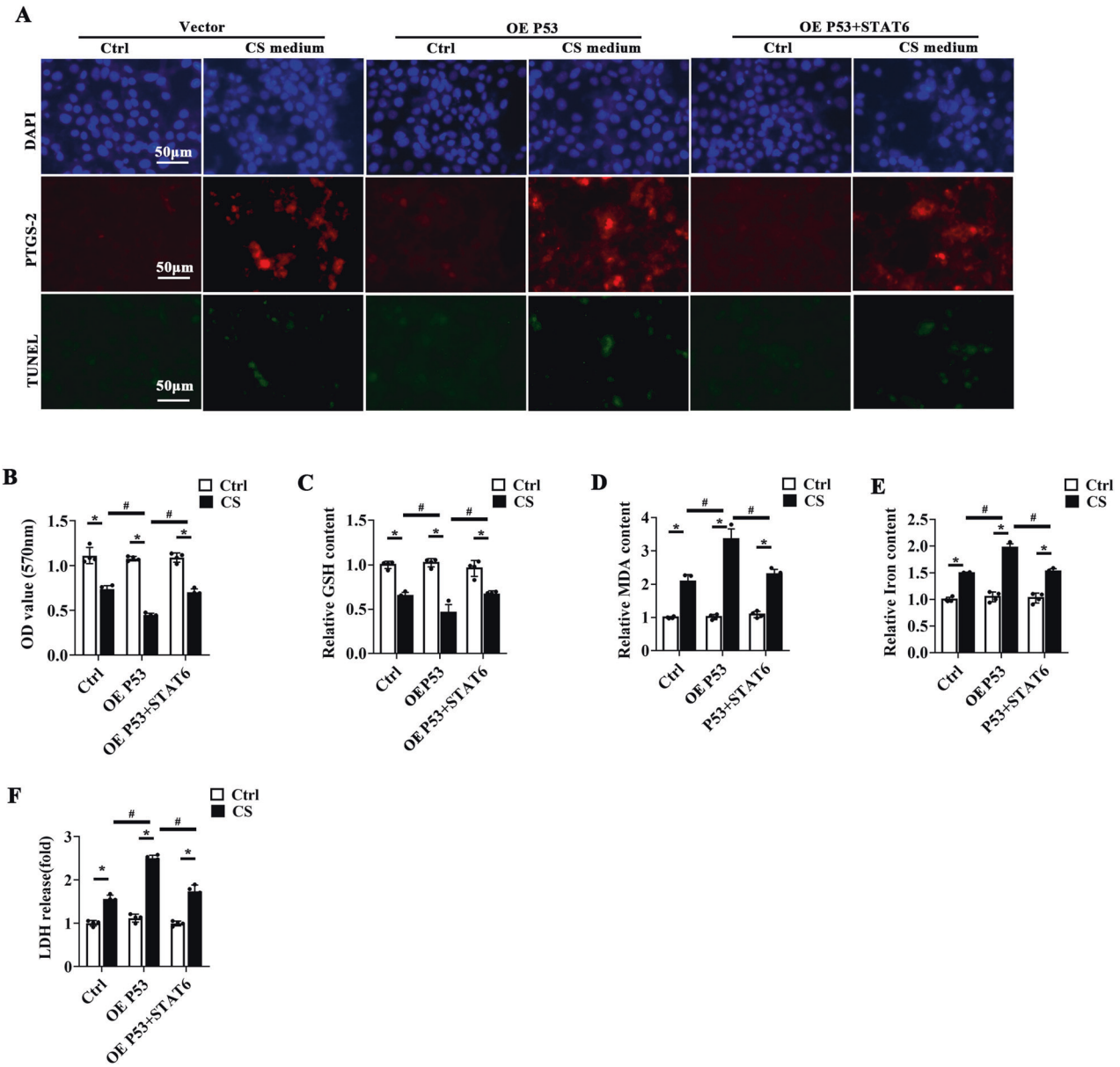

Fig. 5 STAT6 combats P53 overexpression induced cell ferroptosis. HBE cells were transfected with empty vector or plasmids for P53 and/or STAT6 overexpression. Then cells were treated with Ctrl or CS medium for another 24 h. **A** Representative images of PTGS-2 immunofluorescence and TUNEL staining of cells from the indicated group. The cell viability **B**, GSH **C**, MDA **D**, Iron **E** content and LDH release (**F**) of indicated group were measured by corresponding kit. The data were presented as means ± SD ($n = 4$, $^{*}p < 0.05$, Ctrl *vs*. CS; $^{\#}p < 0.05$, P53 + CS *vs*. CS or P53 + STAT6 + CS).

all exacerbated with P53 overexpression, which were alleviated by STAT6 co-transfection. Next, the molecular mechanism of STAT6-induced ferroptosis resistance were further explored. P53 acetylation is the critical modulation related to its interaction with response elements (RE) to regulate its targets transcription, and CBP is the key acetyltransferase for P53 acetylation [49]. The interaction between CBP and STAT6 was first identified (Fig. 6A). Silencing CBP suppressed CS-induced PTGS-2 expression but increased the luciferase activity of SLC7A11 promoter (Fig. 6C–E). Moreover, immunoprecipitation assay suggested that STAT6

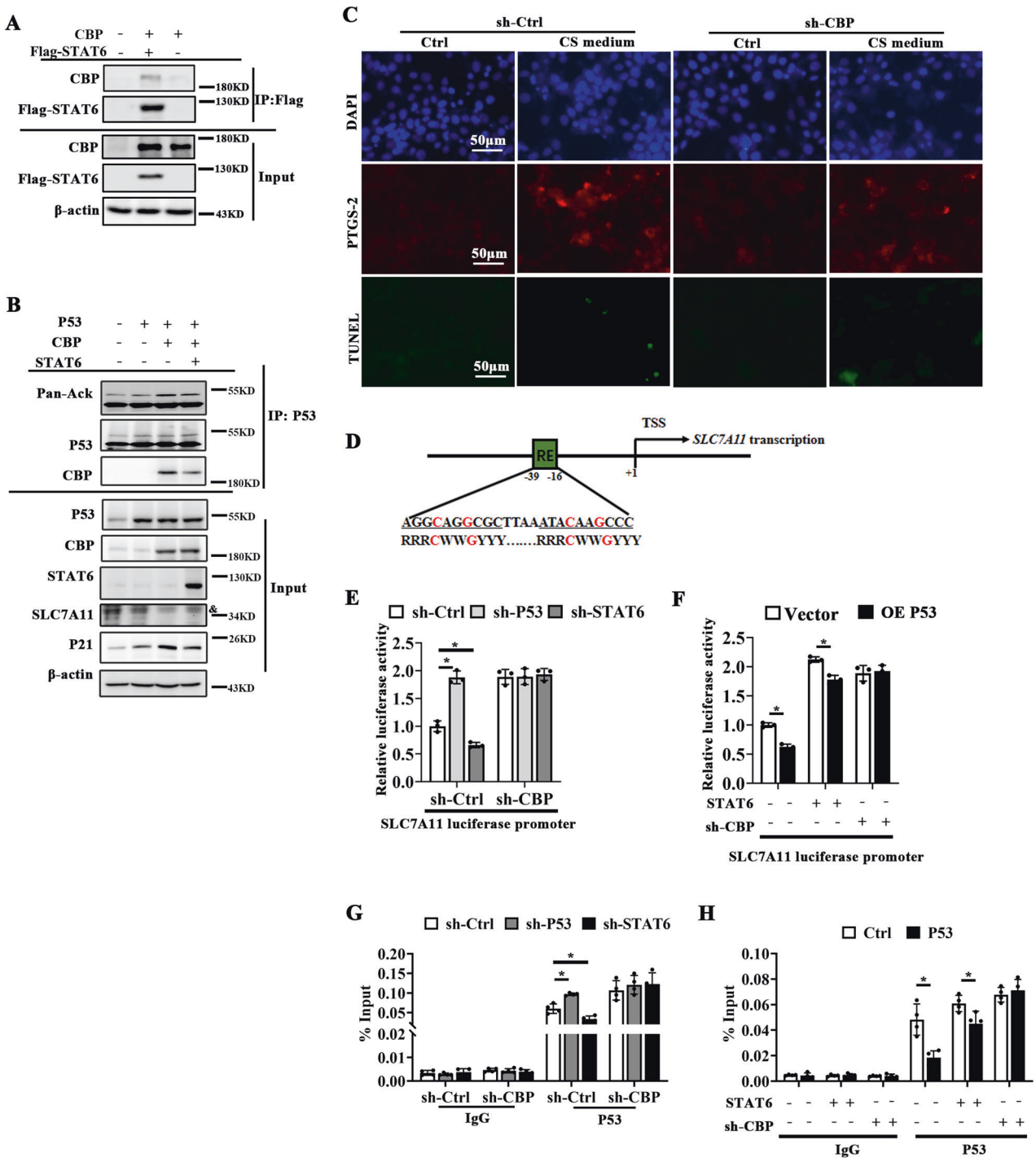

Fig. 6 STAT6 competitively binds with CBP to restore the inhibition of P53 on the expression of SLC7A11. A Cells transfected with difference combination of CBP and Flag-STAT6 were subjected to immunoprecipitation (IP) followed by immunoblot analyses. **B** HBE cells were co-transfected with different combination of P53, CBP, STAT6 as indicated and subjected to immunoprecipitation (IP) followed by immunoblotting (& means the indicated band). **C** Cells transfected with sh-Ctrl or sh-CBP were subjected to immunofluorescence staining of PTGS-2 and TUNEL assay. Representative images were shown. **D** Schematic diagram of P53 binding site and sequence on human SLC7A11 gene. (R, A/G; W, A/T; Y, C/T; nucleotides C and G in red are essential for P53 binding). TSS, transcription start site. **E** HBE cells were transfected with difference combination of sh-CBP, sh-P53, sh-STAT6 accordingly and the luciferase activity of SLC7A11 was detected. Data were presented as means ± SD ($n = 3$, $^*p < 0.05$, Ctrl vs. treatments). **F** The effects of P53 overexpression on the context of STAT6 overexpression or sh-CBP. Luciferase activity of SLC7A11 was determined. The results were presented as means ± SD ($n = 3$, $^*p < 0.05$, Vector *vs.* OE-P53). **G**,**H** The regulation of P53 on SLC7A11 promoter was confirmed by ChIP assay in HBE cells with indicated treatment. Results were expressed as mean ± SD ($n = 4$ $^*p < 0.05$, sh-Ctrl *vs.* sh-P53/sh-STAT6 or Ctrl *vs.* P53 overexpression).

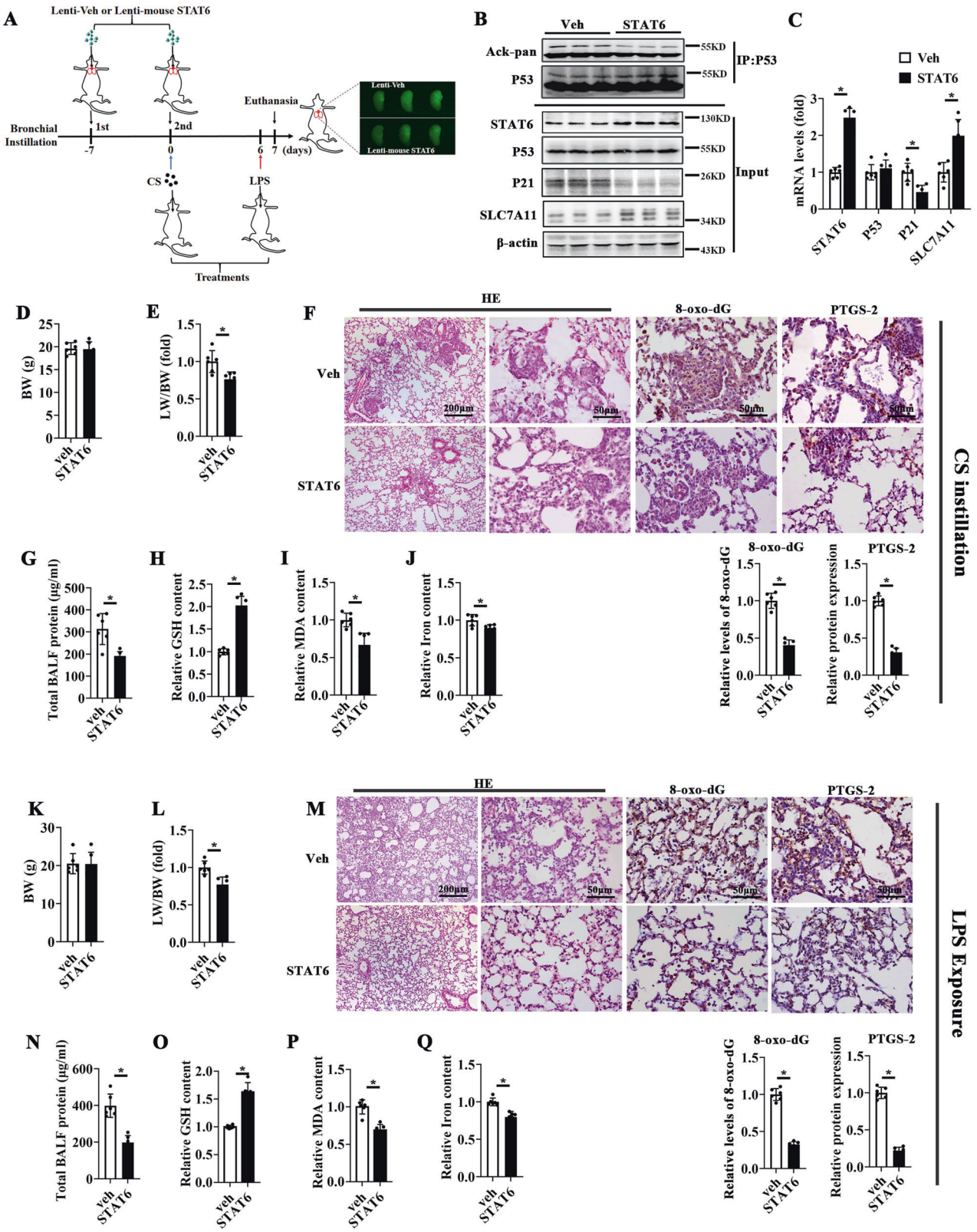

overexpression competitively bound with CBP, decreasing the binding between P53 and CBP, inhibiting P53 acetylation (Fig. 6B). Additionally luciferase reporter assay showed that the inhibited activity of SLC7A11 promoter by P53 were attenuated by STAT6 overexpression or CBP knockdown, which was confirmed by ChIP assay (Fig. 6F–H). Besides, the IP analysis also indicated that knockdown of CBP changed p53 acetylation and SLC7A11 expression (Supplementary Fig. S8E). These data indicates that STAT6 competitively binds with CBP to restore the inhibition of P53 on SLC7A11 expression to improve ferroptosis.

Fig. 7 Rescue of STAT6 attenuates ferroptosis and acute lung injury in both CS- and LPS-induced models. A Timeline of lentivirus transduction with indicated treatment. Mice were intratracheally instilled with lenti-Veh or lenti-mouse STAT6 twice at one week ago and at day 0 respectively. Then Veh and STAT6 mice were bronchially instilled with CS at day 0 or LPS at day 6. All mice were sacrificed at day 7. Lentivius labeled with GFP was successfully instilled as confirmed by the photographs right panel. **B** Lung tissue lysates were harvested and subjected to immunoprecipitation (IP) followed by immunoblot analysis. Representative binds were shown. **C** The mRNA levels of STAT6, P53, P21, SLC7A11 from Veh or STAT6 mice were determined by qRT-PCR assay ($n = 6$). (D-H) Mice were co-treated with lenti-Veh or lenti-mouse STAT6 along with or without CS instillation. Body Weight (**D**) and LW/BW **E** were determined. **F** Representative H&E-stained images and IHC staining of 8-oxo-dG and PTGS-2 of lung sections. Total BALF protein (**G**) and relative GSH **H**, MDA (**I**) and Iron **J** content in lung tissue were measured by corresponding kit. Mice were co-treated with lenti-Veh or lenti-mouse STAT6 along with or without LPS. BW (**K**) and LW/BW **L**, H&E, IHC staining of 8-oxo-dG and PTGS-2 of lung sections **M**, total BALF protein (**N**), and relative GSH **O**, MDA (**P**) and Iron **Q** content in lung tissues. The results were presented as means ± SD ($n = 6$, $^*p < 0.05$, Ctrl *vs*. treatments).

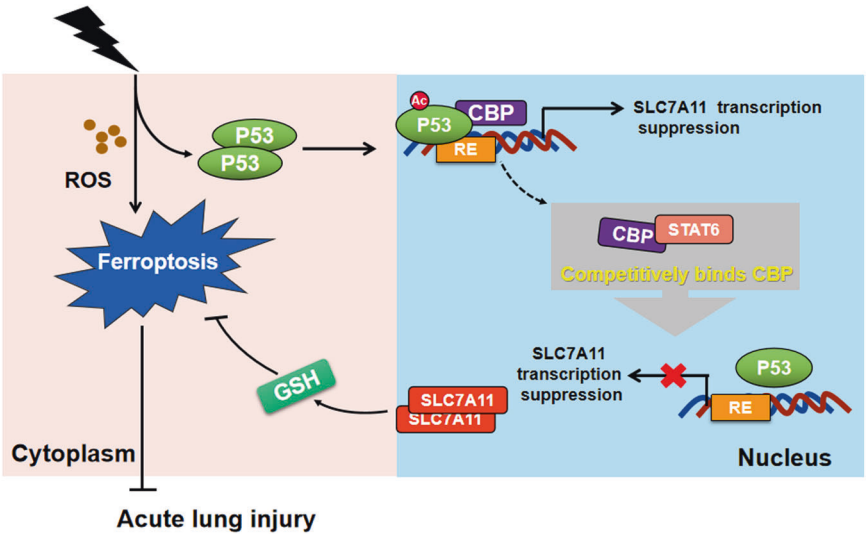

Fig. 8 Proposed model for the regulation of STAT6 on ferroptosis. STAT6 competitively binds with CBP, suppressing the association of P53 and CBP, decreasing the acetylation of P53, restoring SLC7A11 expression and alleviating acute lung injury.

Rescue of STAT6 inhibits ferroptosis and attenuates lung injury in both CS- and LPS-induced models

Next, lentivirus-mediated overexpression of STAT6 were evaluated in CS- and LPS-induced ALI models. The fluorescence images of lung tissues indicated the infection efficiency in both lenti-Veh and lenti-mouse STAT6 groups (Fig. 7A). The expression of STAT6 in the lung tissue of lenti-mouse STAT6 instilled mice was dramatically induced as showed in Fig. 7B, C. And lenti-mouse STAT6 treatment reduced LW/BW (Fig. 7E, L) and BALF protein (Fig. 7G, N). Besides, H&E and IHC staining of 8-oxo-dG showed that the pathological damage and oxidative stress were restored by STAT6 rescue (Fig. 7F, M). Furthermore, STAT6 rescue alleviated CS and LPS caused ferroptosis, manifesting as the decreased expression of PTGS-2 (Fig. 7F, M), the restored GSH content as well as the suppressed content of MDA and iron (Fig. 7H–J, O–Q). These findings indicate that rescue of STAT6 mitigates ferroptosis and improves ALI.

DISCUSSION

Ferroptosis is recently emerging as a new form of cell death, characterized by intracellular iron accumulation and lipid peroxidation [12]. Compelling evidences have indicated the role of ferroptosis in the pathophysiological process of acute injury in multiple tissues especially lung tissue [50–52]. Inhibition ferroptosis could decrease the tissue injury accordingly. Liu et al. reviewed that sevoflurane protects against LPS-induced acute lung injury by inhibiting ferroptosis [53]. Li et al. reported that panaxydol attenuates ferroptosis against LPS-induced acute lung injury in mice [54]. Although studies supported that ferroptosis offers new perspective for the treatment of ALI, whether it is widely existed in most of ALI and its detail regulatory mechanism remains unclear. In this study, Ferr-1 and DFO, as classical inhibitor of ferroptosis, were both used to confirm the significant contribution of ferroptosis to three ALI mice models caused by three common stimuli, including physical factors (CS and X-ray) and biological factor (LPS). All of the three models were detected obvious lung injury, along with increased content of iron and MDA, upregulated expression of PTGS-2 as well as decreased GSH, which were attenuated by Ferr-1 and DFO intervention (Supplementary Figs. S1 and S2). Although TUNEL assay showed that there might be some other forms of cell death during the ALI, ferroptosis still a major contributor as demonstrated by much more positive PTGS-2 staining cells after the stimuli. Thus, exploring the underlying regulation of ferroptosis is imperative for ALI therapeutic strategies development.

STAT6 is a type 2 regulator, and its role in immuno-regulation has been well established. However, its function in intrinsic cells like lung epithelial cells, the most susceptible and the first affected cells during ALI has not been well investigated. Different from the previous studies that STAT6 regulates macrophages clearance of apoptotic neutrophils and resolve LPS-induced ALI [55], here we focused on the regulation of STAT6 on ferroptosis of lung epithelial cells. We originally found that STAT6 expression and activation were upregulated with the increased ferroptosis in the above ALI (Fig. 1). Then the negative association of STAT6 and ferroptosis was further demonstrated through bioinformatic analysis (Figs. 3 and 4).

In order to clarify the impact of STAT6 on ferroptosis of ALI, we generated epithelium-specific STAT6 deficiency mice ($STAT6^{cKO}$). Obviously, $STAT6^{cKO}$ mice exhibited exaggerated ferroptosis and more serious lung injury when exposed to the stimuli (Fig. 2, Supplementary Fig. S5–6). Consistently, STAT6 knockdown in vitro also exhibited more serious damage, while STAT6 overexpression

attenuated the ferroptosis (Fig. 3). These results indicated that STAT6 activation negatively regulates ferroptosis in ALI. On the basis of our current study and previous reports, we thereby proposed that the improvement of STAT6 on ALI may be mostly due to its suppression on epithelium ferroptosis.

The guardian P53, encoded by the TP53 gene, has been primarily linked to its canonical functions including induction of cell-cycle arrest, senescence, and apoptosis [56]. While recent studies have reported the non-canonical functions of P53 such as controlling metabolism and redox state, which are closely related with ferroptosis regulation [57, 58]. P53 has either pro- or anti-ferroptotic functions in response to oxidative stress [59]. Studies have shown that under basal or low ROS stress, P53 might serve as a rheostat by upregulating Nrf2 pathway, preventing ferroptosis. However, under high oxidative stress, the induction of P53 promotes ferroptosis, which always causes the tissue injury [60, 61]. In this study, we consistently found that overexpression P53 promotes HBE cells ferroptosis and deteriorates cell damage (Fig. 5).

Furthermore, it has been reported that P53 sensitizes cells to ferroptosis by transcriptional suppression of SLC7A11, inhibiting the cystine uptake and decreasing the GSH levels [25]. Consistently, we found that P53 was activated in the ALI to trigger ferroptosis in response to ROS stress (Supplementary Fig. S8). Remarkably, previous studies showed that the P53 acetylation is necessary for its regulation on targets. Wang et al. reported that regulation of SLC7A11 expression requires acetylation of the DNA-binding domain of P53 [27]. Unexpectedly, some studies showed that an acetylation defective mutant P53 with three mutated lysines (K117/161/162R) failed to induce apoptosis, senescence, and cell-cycle arrest, but still sensitized the cells to ferroptosis [25, 56]. Alternatively, ectopic expression of the quadruple acetylation defective mutant of P53 in P53-null cells showed that it failed to inhibit SLC7A11 and regulate ferroptosis accordingly [27]. Previous studies have also showed that spermidine/spermine N1-acetyltransferase and CBP are associated with P53 acetylation [62, 63]. Here, we demonstrated that silencing CBP increased SLC7A11 transcription (Fig. 6). Specifically, STAT6 competitively bound with CBP, which suppressed the association of P53 and CBP and decreased the acetylation of P53. Thus, STAT6 negatively regulated ferroptosis via regulating P53/SLC7A11 pathway. In corporation with the induction of P53 in the ALI, modulation intracellular STAT6 was found to attenuate the P53-mediated ferroptosis and increase the cell anti-oxidant capability (Fig. 5).

In summary, our present study originally revealed the competitive binding between STAT6 and CBP, which serves as a crucial event that decreases P53 acetylation, restoring its inhibition on SLC7A11, and finally inhibits ferroptosis (Fig. 8). Our results may provide a potential therapeutic for treating ALI.

DATA AVAILABILITY

The data that support the findings of this study are included in this published article and its supplementary information files are available from the authors on reasonable request, see author contributions for specific data sets.

REFERENCES

1. Ware LB, Matthay MA. The acute respiratory distress syndrome. N Engl J Med. 2000;342:1334–49.
2. Aboushanab SA, El-Far AH, Narala VR, Ragab RF, Kovaleva EG. Potential therapeutic interventions of plant-derived isoflavones against acute lung injury. Int Immunopharmacol. 2021;101:108204.
3. Dushianthan A, Grocott MP, Postle AD, Cusack R. Acute respiratory distress syndrome and acute lung injury. Postgrad Med J. 2011;87:612–22.
4. Matthay MA, Zemans RL, Zimmerman GA, Arabi YM, Beitler JR, Mercat A, et al. Acute respiratory distress syndrome. Nat Rev Dis Prim. 2019;5:18.
5. Beitler JR, Thompson BT, Baron RM, Bastarache JA, Denlinger LC, Esserman L, et al. Advancing precision medicine for acute respiratory distress syndrome. Lancet Respir Med. 2021;10:P107–120.
6. Wu Q, Fang L, Yang Y, Wang A, Chen X, Sun J, et al. Protection of melatonin against long-term radon exposure-caused lung injury. Environ Toxicol. 2021;36:472–83.
7. Tao S, Zhang H, Xue L, Jiang X, Wang H, Li B, et al. Vitamin D protects against particles-caused lung injury through induction of autophagy in an Nrf2-dependent manner. Environ Toxicol. 2019;34:594–609.
8. Lagan AL, Melley DD, Evans TW, Quinlan GJ. Pathogenesis of the systemic inflammatory syndrome and acute lung injury: role of iron mobilization and decompartmentalization. Am J Physiol Lung Cell Mol Physiol. 2008;294:L161–74.
9. Chen X, Kang R. Organelle-specific regulation of ferroptosis. Cell Death Differ. 2021;28:2843–56.
10. Mou Y, Wang J, Wu J, He D, Zhang C, Duan C, et al. Ferroptosis, a new form of cell death: opportunities and challenges in cancer. J Hematol Oncol. 2019;12:34.
11. Badgley MA, Kremer DM. Cysteine depletion induces pancreatic tumor ferroptosis in mice. Science. 2020;368:85–9.
12. Dixon SJ, Lemberg KM, Lamprecht MR, Skouta R, Zaitsev EM, Gleason CE, et al. Ferroptosis: an iron-dependent form of nonapoptotic cell death. Cell. 2012;149:1060–72.
13. Stockwell BR, Jiang X, Gu W. Emerging mechanisms and disease relevance of ferroptosis. Trends Cell Biol. 2020;30:478–90.
14. Kang R, Zhu S, Zeh HJ, Klionsky DJ. BECN1 is a new driver of ferroptosis. Autophagy. 2018;14:2173–5.
15. Xie Y, Hou W, Song X, Yu Y, Huang J, Sun X, et al. Ferroptosis: process and function. Cell Death Differ. 2016;23:369–79.
16. Miess H, Dankworth B, Gouw AM, Rosenfeldt M, Schmitz W, Jiang M, et al. The glutathione redox system is essential to prevent ferroptosis caused by impaired lipid metabolism in clear cell renal cell carcinoma. Oncogene. 2018;37:5435–50.
17. Zhang Z, Guo M, Li Y, Shen M, Kong D, Shao J, et al. RNA-binding protein ZFP36/TTP protects against ferroptosis by regulating autophagy signaling pathway in hepatic stellate cells. Autophagy. 2020;16:1482–505.
18. Hou W, Xie Y, Song X, Sun X, Lotze MT, Zeh HJ 3rd, et al. Autophagy promotes ferroptosis by degradation of ferritin. Autophagy. 2016;12:1425–8.
19. Gaschler MM, Andia AA, Liu H, Csuka JM, Hurlocker B, Vaiana CA, et al. FINO(2) initiates ferroptosis through GPX4 inactivation and iron oxidation. Nat Chem Biol. 2018;14:507–15.
20. NaveenKumar SK, SharathBabu BN, Hemshekhar M, Kemparaju K, Girish KS, Mugesh G. The role of reactive oxygen species and ferroptosis in heme-mediated activation of human platelets. ACS Chem Biol. 2018;13:1996–2002.
21. Bridges RJ, Natale NR, Patel SA. System xc^- cystine/glutamate antiporter: an update on molecular pharmacology and roles within the CNS. Br J Pharmacol. 2012;165:20–34.
22. Hu K, Li K, Lv J, Feng J, Chen J, Wu H, et al. Suppression of the SLC7A11/glutathione axis causes synthetic lethality in KRAS-mutant lung adenocarcinoma. J Clin Investig. 2020;130:1752–66.
23. Liu J, Xia X, Huang P. xCT: a critical molecule that links cancer metabolism to redox signaling. Mol Ther. 2020;28:2358–66.
24. Chen W, Jiang L, Hu Y, Tang N, Liang N, Li XF, et al. Ferritin reduction is essential for cerebral ischemia-induced hippocampal neuronal death through p53/SLC7A11-mediated ferroptosis. Brain Res. 2021;1752:147216.
25. Jiang L, Kon N, Li T, Wang SJ, Su T, Hibshoosh H, et al. Ferroptosis as a p53-mediated activity during tumour suppression. Nature. 2015;520:57–62.
26. Kang R, Kroemer G, Tang D. The tumor suppressor protein p53 and the ferroptosis network. Free Radic Biol Med. 2019;133:162–8.
27. Wang SJ, Li D, Ou Y, Jiang L, Chen Y, Zhao Y, et al. Acetylation is crucial for p53-mediated ferroptosis and tumor suppression. Cell Rep. 2016;17:366–73.
28. Czimmerer Z, Daniel B, Horvath A, Rückerl D, Nagy G, Kiss M, et al. The transcription factor STAT6 mediates direct repression of inflammatory enhancers and limits activation of alternatively polarized macrophages. Immunity. 2018;48:75–90.e6.
29. Hu X, Wang H, Han C, Cao X. Src promotes anti-inflammatory (M2) macrophage generation via the IL-4/STAT6 pathway. Cytokine. 2018;111:209–15.
30. Li Y, Sheng Q, Zhang C, Han C, Bai H, Lai P, et al. STAT6 up-regulation amplifies M2 macrophage anti-inflammatory capacity through mesenchymal stem cells. Int Immunopharmacol. 2021;91:107266.
31. Yang F, Cai H, Zhang X, Sun J, Feng X, Yuan H, et al. An active marine halophenol derivative attenuates lipopolysaccharide-induced acute liver injury in mice by improving M2 macrophage-mediated therapy. Int Immunopharmacol. 2021;96:107676.
32. Li J, Yang Y, Wei S, Chen L, Xue L, Tian H, et al. Bixin protects against kidney interstitial fibrosis through promoting STAT6 degradation. Front Cell Dev Biol. 2020;8:576988.
33. Matute-Bello G, Downey G, Moore BB, Groshong SD, Matthay MA, Slutsky AS, et al. An official American Thoracic Society workshop report: features and measurements of experimental acute lung injury in animals. Am J Respir Cell Mol Biol. 2011;44:725–38.
34. Zhang W, Wang Y, Li C, Xu Y, Wang X, Wu D, et al. Extracellular CIRP-impaired Rab26 restrains EPOR-mediated macrophage polarization in acute lung injury. Front Immunol. 2021;12:768435.

35. Tao S, Wang S, Moghaddam SJ, Ooi A, Chapman E, Wong PK, et al. Oncogenic KRAS confers chemoresistance by upregulating NRF2. Cancer Res. 2014;74:7430–41.
36. Edgar R, Domrachev M, Lash AE. Gene Expression Omnibus: NCBI gene expression and hybridization array data repository. Nucleic acids Res. 2002;30:207–10.
37. Human genomics. The Genotype-Tissue Expression (GTEx) pilot analysis: multitissue gene regulation in humans. Science. 2015;348:648–60.
38. Phipson B, Lee S, Majewski IJ, Alexander WS, Smyth GK. Robust hyperparameter estimation protects against hypervariable genes and improves power to detect differential expression. Ann Appl Stat. 2016;10:946–63.
39. Ritchie ME, Phipson B, Wu D, Hu Y, Law CW, Shi W, et al. limma powers differential expression analyses for RNA-sequencing and microarray studies. Nucleic Acids Res. 2015;43:e47.
40. Gu Z, Eils R, Schlesner M. Complex heatmaps reveal patterns and correlations in multidimensional genomic data. Bioinforma. 2016;32:2847–9.
41. Durinck S, Moreau Y, Kasprzyk A, Davis S, De Moor B, Brazma A, et al. BioMart and Bioconductor: a powerful link between biological databases and microarray data analysis. Bioinforma. 2005;21:3439–40.
42. Durinck S, Spellman PT, Birney E, Huber W. Mapping identifiers for the integration of genomic datasets with the R/Bioconductor package biomaRt. Nat Protoc. 2009;4:1184–91.
43. Szklarczyk D, Gable AL, Lyon D, Junge A, Wyder S, Huerta-Cepas J, et al. STRING v11: protein-protein association networks with increased coverage, supporting functional discovery in genome-wide experimental datasets. Nucleic Acids Res. 2019;47:D607–d13.
44. Shannon P, Markiel A, Ozier O, Baliga NS, Wang JT, Ramage D, et al. Cytoscape: a software environment for integrated models of biomolecular interaction networks. Genome Res. 2003;13:2498–504.
45. Tonnus W, Meyer C. Dysfunction of the key ferroptosis-surveilling systems hypersensitizes mice to tubular necrosis during acute kidney injury. Nat Commun. 2021;12:4402.
46. Jahn HM, Kasakow CV, Helfer A, Michely J, Verkhratsky A, Maurer HH, et al. Refined protocols of tamoxifen injection for inducible DNA recombination in mouse astroglia. Sci Rep. 2018;8:5913.
47. Wu G, Wang Q, Xu Y, Li Q, Cheng L. A new survival model based on ferroptosis-related genes for prognostic prediction in clear cell renal cell carcinoma. Aging. 2020;12:14933–48.
48. Yu T, Gan S, Zhu Q, Dai D, Li N, Wang H, et al. Modulation of M2 macrophage polarization by the crosstalk between Stat6 and Trim24. Nat Commun. 2019;10:4353.
49. Gaub P, Tedeschi A, Puttagunta R, Nguyen T, Schmandke A, Di Giovanni S. HDAC inhibition promotes neuronal outgrowth and counteracts growth cone collapse through CBP/p300 and P/CAF-dependent p53 acetylation. Cell Death Differ. 2010;17:1392–408.
50. Yoshida M, Minagawa S. Involvement of cigarette smoke-induced epithelial cell ferroptosis in COPD pathogenesis. Nat Commun. 2019;10:3145.
51. Zhang X, Ding M, Zhu P. New insights into the Nrf-2/HO-1 signaling axis and its application in pediatric respiratory diseases. Oxid Med Cell Longev. 2019;2019:3214196.
52. Friedmann Angeli JP, Schneider M, Proneth B, Tyurina YY, Tyurin VA, Hammond VJ, et al. Inactivation of the ferroptosis regulator Gpx4 triggers acute renal failure in mice. Nat Cell Biol. 2014;16:1180–91.
53. Liu X, Wang L, Xing Q, Li K, Si J, Ma X, et al. Sevoflurane inhibits ferroptosis: a new mechanism to explain its protective role against lipopolysaccharide-induced acute lung injury. Life Sci. 2021;275:119391.
54. Li J, Lu K, Sun F, Tan S, Zhang X, Sheng W, et al. Panaxydol attenuates ferroptosis against LPS-induced acute lung injury in mice by Keap1-Nrf2/HO-1 pathway. J Transl Med. 2021;19:96.
55. Nepal S, Tiruppathi C, Tsukasaki Y, Farahany J, Mittal M, Rehman J. STAT6 induces expression of Gas6 in macrophages to clear apoptotic neutrophils and resolve inflammation. Proc Natl Acad Sci USA. 2019;116:16513–8.
56. Li T, Kon N, Jiang L, Tan M, Ludwig T, Zhao Y, et al. Tumor suppression in the absence of p53-mediated cell-cycle arrest, apoptosis, and senescence. Cell. 2012;149:1269–83.
57. Bieging KT, Mello SS, Attardi LD. Unravelling mechanisms of p53-mediated tumour suppression. Nat Rev Cancer. 2014;14:359–70.
58. Kaiser AM, Attardi LD. Deconstructing networks of p53-mediated tumor suppression in vivo. Cell Death Differ. 2018;25:93–103.
59. Gnanapradeepan K, Basu S, Barnoud T, Budina-Kolomets A, Kung CP, Murphy ME. The p53 tumor suppressor in the control of metabolism and ferroptosis. Front Endocrinol. 2018;9:124.
60. Kruiswijk F, Labuschagne CF, Vousden KH. p53 in survival, death and metabolic health: a lifeguard with a licence to kill. Nat Rev Mol Cell Biol. 2015;16:393–405.
61. Li Y, Cao Y, Xiao J, Shang J, Tan Q, Ping F, et al. Inhibitor of apoptosis-stimulating protein of p53 inhibits ferroptosis and alleviates intestinal ischemia/reperfusion-induced acute lung injury. Cell Death Differ. 2020;27:2635–50.
62. Ou Y, Wang SJ, Li D, Chu B, Gu W. Activation of SAT1 engages polyamine metabolism with p53-mediated ferroptotic responses. Proc Natl Acad Sci USA. 2016;113:E6806–e12.
63. Juillard F, de Miranda MP, Li S, Franco A. KSHV LANA acetylation-selective acidic domain reader sequence mediates virus persistence. Proc Natl Acad Sci USA. 2020;117:22443–51.

ACKNOWLEDGEMENTS

The grants that supported our study are as follows: National Natural Science Foundation of China (Grant ref: 81703205); A project funded by the Priority Academic Program Development of Jiangsu Higher Education Institutions (PAPD); Foundation from Chongqing Yuzhong District Science and Technology Bureau (201930) and the Natural Science Foundation of Chongqing Science and Technology Bureau (cstc2020jcyj-msxm3187, cstc2020jcyj-msxm3430).

AUTHOR CONTRIBUTIONS

YY and YM: designed the experiments and performed part of the experiments. QL: performed part of the experiments. YL: software, investigation. YZ provided technical and material support. KC and LX: performed and analyzed the result of mouse model. ST: conceptualization, visualization, writing-review & editing, supervision, project administration. All authors read and approved the final paper.

COMPETING INTERESTS

The authors declare no competing interests.

ADDITIONAL INFORMATION

Supplementary information The online version contains supplementary material available at https://doi.org/10.1038/s41419-022-04971-x.

Correspondence and requests for materials should be addressed to Shasha Tao.

Reprints and permission information is available at http://www.nature.com/reprints

Publisher's note Springer Nature remains neutral with regard to jurisdictional claims in published maps and institutional affiliations.